Article (refereed) – Published version

Hodell, David; Crowhurst, Simon; Skinner, Luke; Tzedakis, Polychronis C.; Margari, Vasiliki; Channell, James E.T.; Kamenov, George; Maclachlan, Suzanne; Rothwell, Guy. 2013 Response of Iberian Margin sediments to orbital and suborbital forcing over the past 420 ka. *Paleoceanography*, 28 (1). 185-199. 10.1002/palo.20017

Response of Iberian Margin sediments to orbital and suborbital forcing over the past 420 ka

David Hodell,[1] Simon Crowhurst,[1] Luke Skinner,[1] Polychronis C. Tzedakis,[2] Vasiliki Margari,[2] James E.T. Channell,[3] George Kamenov,[3] Suzanne Maclachlan,[4] and Guy Rothwell[4]

[1] Here we report 420 kyr long records of sediment geochemical and color variations from the southwestern Iberian Margin. We synchronized the Iberian Margin sediment record to Antarctic ice cores and speleothem records on millennial time scales and investigated the phase responses relative to orbital forcing of multiple proxy records available from these cores. Iberian Margin sediments contain strong precession power. Sediment "redness" (a* and 570–560 nm) and the ratio of long-chain alcohols to n-alkanes ($C_{26}OH/(C_{26}OH + C_{29})$)) are highly coherent and in-phase with precession. Redder layers and more oxidizing conditions (low alcohol ratio) occur near precession minima (summer insolation maxima). We suggest these proxies respond rapidly to low-latitude insolation forcing by wind-driven processes (e.g., dust transport, upwelling, precipitation). Most Iberian Margin sediment parameters lag obliquity maxima by 7–8 ka, indicating a consistent linear response to insolation forcing at obliquity frequencies driven mainly by high-latitude processes. Although the lengths of the time series are short (420 ka) for detecting 100 kyr eccentricity cycles, the phase relationships support those obtained by *Shackleton* [2000]. Antarctic temperature and the Iberian Margin alcohol ratios ($C_{26}OH/(C_{26}OH + C_{29})$)) lead eccentricity maxima by 6 kyr, with lower ratios (increased oxygenation) occurring at eccentricity maxima. CO_2, CH_4, and Iberian SST are nearly in phase with eccentricity, and minimum ice volume (as inferred from Pacific $\delta^{18}O_{seawater}$) lags eccentricity maxima by 10 kyr. The phase relationships derived in this study continue to support a potential role of the Earth's carbon cycle in contributing to the 100 kyr cycle.

1. Introduction

[2] In 1976, Hays, Imbrie, and Shackleton published their seminal paper on "Variations in the Earth's Orbit: Pacemaker of the Ice Ages" in which they showed that periodicities predicted by *Milankovitch* [1941] are indeed present in the deep-sea sediment record. *Hays et al.* [1976] identified two primary obstacles to testing the Milankovitch hypothesis. The first was identifying which aspects of the climate system are most sensitive to changes in seasonal anomalies induced by orbital geometry. The second was uncertainty associated with chronology. Although we have made strides toward understanding the orbital effects on climate and in dating of paleoclimate archives, a complete theory of the ice ages still remains elusive [*Raymo and Huybers*, 2008].

[3] With regard to the first obstacle, two complementary approaches have been taken to understand the sequence of climate responses and feedbacks to insolation forcing. The first is a time-domain approach whereby the timing of changes in the ocean-atmosphere system is compared to insolation forcing (e.g., across glacial terminations). The second is a frequency-domain approach whereby the amplitude and phase of the climate system's response are compared to the forcing for each of the orbital cycles. The latter is illustrated by the seminal work of *Imbrie et al.* [1992, 1993] who used the phase progression in each climatic cycle to propose a mechanism by which the initial boreal summer insolation forcing triggers a sequence of climatic responses and

---

feedbacks that are propagated through the ocean-atmosphere system, ultimately giving rise to ice volume changes.

[4] The two approaches each have their merits and short-comings [*Alley et al.*, 1989; *Ruddiman*, 2006], and both require precise stratigraphic correlation of marine and ice core records and construction of an absolute time scale that is accurate relative to changes in orbital geometry. Most marine sediment chronologies are derived by correlating benthic oxygen isotope variation to a reference stack, such as SPECMAP [*Imbrie et al.*, 1984] or LR04 [*Lisiecki and Raymo*, 2005]. These reference chronologies have been established by correlating the stacked benthic δ^{18}O signal to the output of an ice volume model [*Imbrie and Imbrie*, 1980], assuming the stack represents global changes in the δ^{18}O of seawater. There are two problems with this approach: (1) chronologies based on oxygen isotope stratigraphy contain inherent assumptions about the lag between insolation forcing and ice-sheet response, and (2) benthic δ^{18}O is not an unambiguous proxy for ice volume [*Shackleton*, 2000; *Elderfield et al.*, 2010, 2012].

[5] Several attempts have been made to solve the first problem by developing time scales that are independent of δ^{18}O reference curves, thereby relaxing the assumption of fixed lags [e.g., *Huybers*, 2006; *Shackleton*, 2000]. Here we present an independent chronology for sediment cores from the southwest Iberian Margin by correlating millennial-scale events to the globally integrated event stratigraphy of *Barker et al.* [2011], which is tied to a radiometric-based speleothem chronology. The second problem is addressed by using a benthic δ^{18}O record from ODP Site 1123 that has been deconvolved into its temperature and δ^{18}O$_{water}$ components [*Elderfield et al.*, 2012].

[6] Although millennial-scale variations have been well studied using Iberian Margin piston cores [for review, see *Voelker and deAbreu*, 2011], orbital-scale variations have received less attention. Here we use millennial variability to synchronize the Iberian Margin sediment record to Antarctic ice core and speleothem records and then determine the spectral properties of these records to study the phase responses of proxy signals relative to orbital forcing.

2. Iberian Margin Cores

[7] Sediments on the southwestern Iberian Margin are highly responsive to climate change on both millennial and orbital timescales. First, they have high and relatively constant sedimentation rates that are maintained through glacial-interglacial and stadial-interstadial periods. Second, the Iberian Margin is sensitive climatically because it is influenced by both high- and low-latitude processes. Migrations of the Polar Front in the North Atlantic act as a hinge with a pivot in the western basin, with large meridional swings occurring in the eastern basin as sea ice advances and retreats. During the coldest (Heinrich) stadials of the last glacial period, the polar front reached the northern Iberian margin (~41°N) [*Voelker and deAbreu*, 2011]. The Iberian Margin is also influenced by low-latitude processes, mainly through the hydrological cycle as precipitation over Europe shifts with migration of the position of the Intertropical Convergence on orbital and millennial timescales [*Tzedakis et al.*, 2009].

[8] Third, sediment cores from the Iberian margin are unique in their ability to be correlated to polar ice cores in both hemispheres and with European terrestrial sequences. In Core MD95-2042, variations in planktic δ^{18}O and SST record all of the Dansgaard-Oeschger (D-O) events of the last glacial period and can be correlated unambiguously to the Greenland ice core δ^{18}O records [*Shackleton et al.*, 2000; *Martrat et al.*, 2007; *Skinner et al.*, 2007]. In contrast, the benthic δ^{18}O curve resembles the temperature record from Antarctica, both in its shape and phasing relative to Greenland and North Atlantic surface temperature records [*Shackleton et al.*, 2000, 2004]. Moreover, the narrow continental shelf and proximity of the Tagus River result in the rapid delivery of terrestrial material, including pollen, to the deep-sea environment, thereby permitting direct correlation to European terrestrial sequences. In addition to millennial-scale variations, Iberian margin sediments also preserve a longer record of the late Pleistocene orbital-scale fluctuations [*Thomson et al.*, 1999; *Shackleton et al.*, 2002; *Tzedakis et al.*, 2004, 2009; *Voelker and de Abreu*, 2011]. For all these reasons, the Iberian Margin has become a focal point for studies of past climate variability over the last several glacial cycles. Thus, it is important to identify the processes responsible for imprinting these orbital and millennial signals on the sediment record.

[9] Several expeditions to the Iberian Margin aboard the R/V *Marion Dufresne* have recovered a suite of high-quality cores using the Calypso long-core system. Here we studied Cores MD01-2443 (37°52.89′N, 10°10.57′W, 2952 m water depth) and MD01-2444 (37°33.88′N, 10°8.34′W, 2656 m water depth) that were obtained from a spur on the upper slope that is elevated above the abyssal plain on the continental rise (Figure 1). Core MD01-2444 is 27 m long and contains a record of the last 194 kyr to Marine Isotope Stage (MIS) 7 with a mean sedimentation rate of 14 cm kyr^{-1} [*Margari et al.*, 2010]. Core MD01-2443 is 29.5 m long and extends back to MIS 11 with a mean sedimentation rate of 5.8 cm kyr^{-1} between 194 and 424 ka [*de Abreu et al.*, 2005].

[10] The two cores were spliced by appending data from MD01-2443 to the bottom of MD01-2444, which results in a continuous record to 424 ka. The splice tie point corresponds to a depth of 27.42 meters below sea floor (mbsf) in MD01-2444 and 16.74 mbsf in Core MD01-2443, equivalent to an age of ~194 ka. The two cores have been used extensively for paleoceanographic studies with detailed records of faunal counts, stable isotopes, organic biomarkers, and pollen [for review, see *Voelker and de Abreu*, 2011, and references therein].

[11] One of the rationales for this work was to provide a basis for interpreting the longer record obtained at Site U1385, which was drilled at the same location as Core MD01-2444. During IODP Expedition 339, a continuous ~1.4 Myr long sediment record was recovered in five holes with an average sedimentation rate of ~10 cm kyr^{-1} [*Stow et al.*, 2012].

3. Methods

3.1. XRF Analysis

[12] Core scanning XRF offers a rapid, non-destructive method for semi-quantitatively determining variations in elemental composition along a core surface. Archive halves of 19 sections from Core MD01-2444 and 20 sections from MD01-2443 were analyzed using an Avaatech XRF core scanner at the University of Cambridge. The core surface was carefully scraped cleaned and covered with a 4 µm thin SPEXCertiPrep Ultralene foil to avoid contamination and
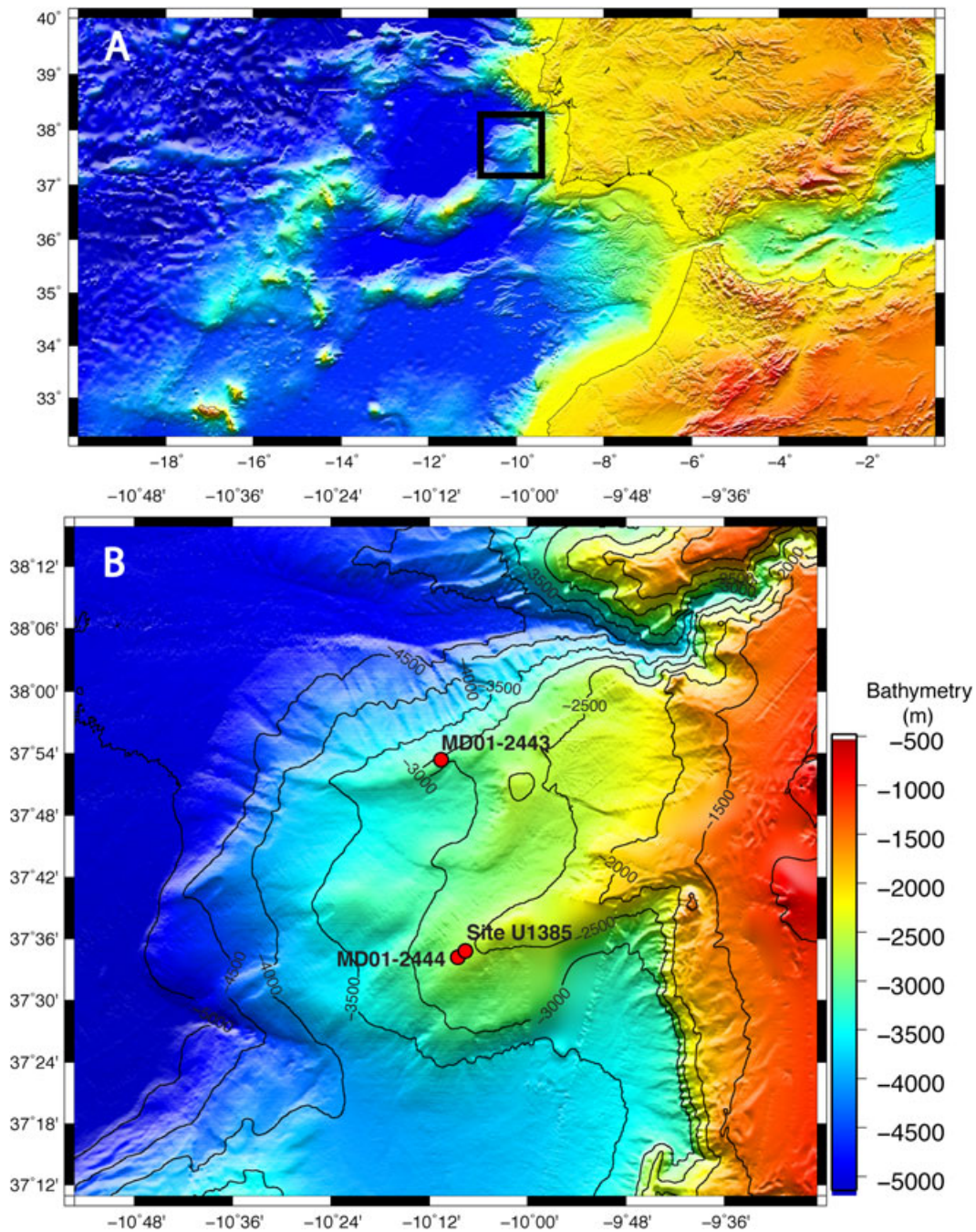
Figure 1. Maps of (a) West Iberian margin showing (b) detailed bathymetry and locations of Marion Dufresne (MD) piston cores MD01-2443 and -2444, and IODP Site U1385. Modified after *Expedition 339 Scientists* [2012].

minimize desiccation [*Richter and van der Gaast*, 2006]. Each section was measured using a current of 0.2 mA at three different voltages: 10 kilovolts (kV), 30 kV using a thin lead filter, and 50 kV using a copper filter. XRF data were collected every 2.5 mm along the entire length of the two cores. The length and width of the irradiated surface was 2.5 and 12 mm, respectively, with a count time of 40 s. Results are presented in log ratios of element intensities, which best reflect changes in chemical composition [*Weltje and Tjallingii*, 2008].

3.2. Color Reflectance

[13] Diffuse color reflectance was measured every 5 mm using a Minolta spectrophotometer mounted on a GEOTEK XYZ multi-sensor core logger (MSCL-XYZ) at the British Ocean Sediment Core Research Facility (BOSCORF), National Oceanography Centre, Southampton. The color spectrum for each measurement ranges from 360 to 740 nm binned in 10 nm intervals. We used the CIELAB system where L* is the lightness varying between 0 and 100%, a* is the red

(positive) to green (negative) axis, and b* is the yellow (positive) to blue (negative) axis.

3.3. Carbonate Content

[14] Weight percent $CaCO_3$ was measured on ~700 samples to calibrate the XRF data. Bulk sediment was acidified with 10% phosphoric acid using an AutoMateFX carbonate preparation system and evolved CO_2 was measured using a UIC (Coulometrics) 5011 CO_2 coulometer. Analytical precision is estimated to be ±1% by repeated measurement of a carbonate standard.

3.4. Stable Isotopes

[15] Bulk oxygen and carbon isotopes of carbonate were measured using a ThermoFisher GasBench II equipped with a CTC Combi-Pal autosampler and interfaced via continuous flow with a ThermoFisher MAT 253 isotope ratio mass spectrometer (IRMS). About 200–300 μg of bulk sample was loaded into 10 mL Exetainer tubes (Labco Limited) and sealed with butyl rubber septa. The vials were flushed with helium prior to reaction with 100% ortho-phosphoric acid. The resulting CO_2 was analyzed by repetitive loop injections onto an isothermal GC column producing pulses of CO_2 in He that are introduced to the IRMS via an open split. Analytical precision is estimated to be ±0.08‰ for $\delta^{18}O$ and ±0.06‰ for $\delta^{13}C$ based on routine measurement of an internal standard (Carrara marble).

[16] Bulk samples for strontium isotope analysis were treated with ultrapure 1 M acetic acid to dissolve carbonate but not leach the silicate sediment fraction. The leachate was dried and dissolved in HNO_3. Strontium was separated from other cations by passing the sample through micro-columns containing strontium-specific crown resin (EichromTM Sr resin) [*Pin and Bassin*, 1992]. Strontium isotope ratios were measured on a Nu-Plasma MC-ICP-MS using a protocol for highly precise measurements of small samples described by *Kamenov et al.* [2009]. $^{87}Sr/^{86}Sr$ values were normalized to $^{86}Sr/^{88}Sr = 0.1194$ and ^{87}Sr was corrected for isobaric interference by Rb by subtracting the counts of ^{87}Rb expected given an $^{87}Rb/^{85}Rb$ of 0.386. The long-term mean $^{87}Sr/^{86}Sr$ ratio of the standard NBS 987 is 0.710246 (±0.000030, 2σ).

3.5. Magnetic Measurements

[17] Details of magnetic measurements on u-channel samples ($2 \times 2 \times 150 \, cm^3$ continuous samples encased in plastic) collected from archive sections of Core MD01-2444 are described by J. E. T. Channell et al. (Relative paleointensity (0-420 ka) and biogenic magnetite in sediments from the Southwest Iberian Margin, submitted to *Earth and Planetary Science Letters*, 2013). Isothermal remanent magnetization ($IRM_{0.3T}$) was acquired using a DC impulse field of 0.3 T, then stepwise demagnetized using alternating fields, and then an additional IRM_{1T}, acquired in impulse fields of 1 T, was demagnetized once more in the same peak demagnetization fields. The measurement $IRM_{0.3T}$ and IRM_{1T}, allows us to calculate a "forward S-ratio" [see *Bloemendal et al.*, 1988, 1992; *Heslop*, 2009] calculated as the ratio $IRM_{0.3T}/ IRM_{1T}$. The S-ratio, as determined here, is sensitive to the concentration of magnetic minerals with coercivities >0.3 T, such as hematite and goethite.

3.6. Age Model

[18] The age model is a modified version of the one derived by *Barker et al.* [2011] based on correlation of millennial variability in MD01-2444 and MD01-2443 records to a synthetic Greenland temperature record produced using the EPICA Dome C (EDC) ice core and placed on the absolute "Speleo-Age" timescale. The age model justification is based on the unambiguous correlation of planktic $\delta^{18}O$ and SST records from Iberian margin cores with temperature variations in Greenland during the last glacial period [*Shackleton et al.*, 2000, 2004]. In particular, we correlated millennial-scale cold events in the planktic $\delta^{18}O$ and SST signals to the synthetic Greenland temperature record of *Barker et al.* [2011] (Figure 3). This timescale integrates three event stratigraphies: the Greenland ice core, the Antarctic ice core, and the Asian speleothem record, which possesses an "absolute" age-scale based on uranium-series dating. The synthetic Greenland record was placed on the "Speleo-Age" timescale by correlating cold events in Greenland with "weak monsoon events" in the detrended speleothem record [*Barker et al.*, 2011]. Thus, we are able to tie the Iberian Margin sediment record to this globally integrated event stratigraphy that is independent of the LR04 oxygen isotope stack [*Lisiecki and Raymo*, 2005]. The precise synchronization of the Iberian Margin sediment record to Antarctic ice cores and speleothem records on millennial time scales then permit us to investigate the phase responses of proxy records relative to orbital forcing.

3.7. Time Series Analysis

[19] Spectral and cross-spectral analysis was performed to test for statistically significant cycles, coherence, and phase of proxy signals with respect to orbital parameters and other global records. For analysis of orbital periodicities, all time series were resampled at a constant time step of 1 kyr, linearly detrended, and normalized to unit variance. The ARAND software package was used for spectral and cross-spectral estimates [*Howell et al.*, 2006]. For suborbital periodicities, non-constantly sampled time series were analyzed by a multitaper method using the program REDFIT [*Schulz and Mudelsee*, 2002].

4. Results

4.1. XRF

[20] Log (Ca/Ti) is well correlated with weight percent $CaCO_3$ ($r = 0.91$) with generally higher values during interglacials and interstadials and lower values during glacials and stadials (Figure 2). Millennial-scale variations in Ca/Ti follow planktic $\delta^{18}O$ and alkenone SST and resemble in great detail the Greenland ice core $\delta^{18}O$ record for the last glacial period, capturing most of the Dansgaard-Oeschger events (Figure 3). Millennial-scale variability in Ca/Ti continues beyond 70 kyr, but is overprinted by a stronger precession cycle. From 70 to 274 ka, Ca/Ti variations are of similar amplitude with a strong cyclicity centered at ~22 kyr. Beginning with MIS 9a (274 ka), the amplitude of the Ca/Ti signal increases and interglacial peaks remain high to the base of the record.

[21] To emphasize the millennial-scale variability, we removed the longer-term trends by subtracting a weighted curve fit (Lowess method) from the Ca/Ti signal (see Supporting Information). The residual signal bears a strong
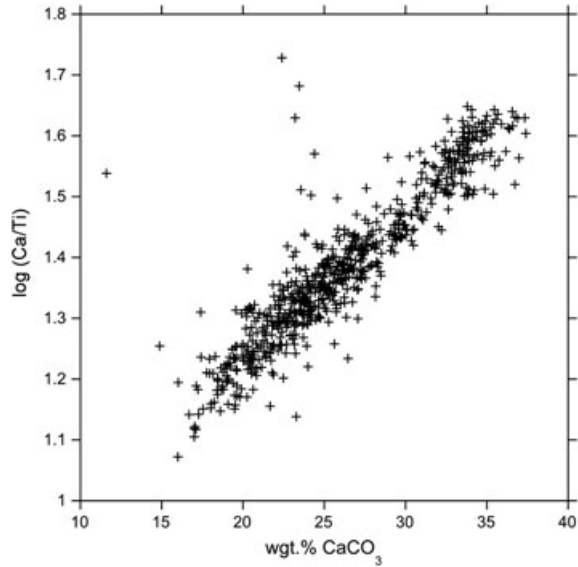
Figure 2. Weight percent calcium carbonate versus log (Ca/Ti) measured by core scanning XRF.

resemblance to the synthetic Greenland high-frequency curve of *Barker et al.* [2011] (Figure 4). A power spectrum of the Ca/Ti residual using the multitaper method (REDFIT) shows peaks at 23, 15, 12, 9, 6, 5, 4, and 3 kyr [*Schulz and Mudelsee*, 2002] (Figure 5). The 23 kyr cycle corresponds to precession and some of the higher frequency peaks may represent harmonics of the precession cycle.

[22] Peaks in barium concentration occur on each of the glacial terminations (I–IV) of the past 400 kyr (Figure 6), as described previously in cores from the Iberian Margin [*Thomson et al.*, 2000].

4.2. Color Reflectance

[23] Sediments consist of greenish-gray (10Y 5/1) hemipelagic nannofossil mud and clays, with distinct bioturbation and varying proportions of carbonate. The most obvious variations visually are changes in sediment lightness (L*), but variations in redness are also evident (Figure 7). Variations in redness are expressed as a* (red-green) with higher values corresponding to redder color. The primary mineral imparting the red color to the sediment is hematite, which is marked by a diagnostic peak in the first derivative of the color spectrum between 555 and 575 nm [*Barranco et al.*, 1989; *Deaton and Balsam*, 1991]. Both a* and the hematite proxy (570–560 nm) show very strong cyclic variations for orbital precession (19–23 ka) and eccentricity (~100 kyr), but no power in the obliquity (41 kyr) band (see Supporting Information).

5. Discussion

5.1. Causes of Ca/Ti Variations

[24] Variations in log (Ca/Ti) provide a reliable proxy for weight %CaCO$_3$ (Figure 2) and reflect varying proportions of biogenic (Ca) and detrital (Ti) sediment supply. Higher Ca/Ti occurs during interglacial and interstadial stages whereas lower values are found during glacial and stadial periods. *Thomson et al.* [1999] measured excess ^{230}Th and calculated carbonate accumulation rates in cores from the Iberian Margin. They showed carbonate accumulation rates remained relatively constant across glacial-interglacial cycles but clay accumulation varied greatly. They ascribed orbital periodicities observed in weight %CaCO$_3$ to variable dilution by clays rather than changes in carbonate productivity. Clay flux increased during sea level lowstands and decreased during highstands owing to trapping of river-derived clays
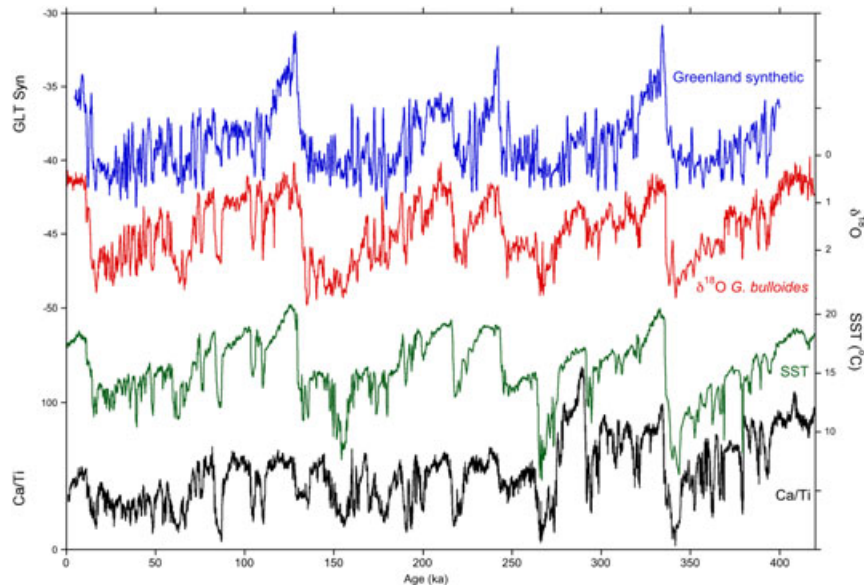
Figure 3. Ca/Ti (black; log scale), alkenone sea surface temperature (Uk'$_{37}$; green) [*Martrat et al.*, 2007], δ^{18}O of *G. bulloides* (red) [*de Abreu et al.*, 2005; *Vautravers and Shackleton*, 2006] from the combined record of Core MD01-2444 (0–194 ka) and MD01-2443 (194–420 ka), and the Greenland synthetic δ^{18}O record (blue) [*Barker et al.*, 2011]. There are strong similarities of the orbital and suborbital variations among the records.
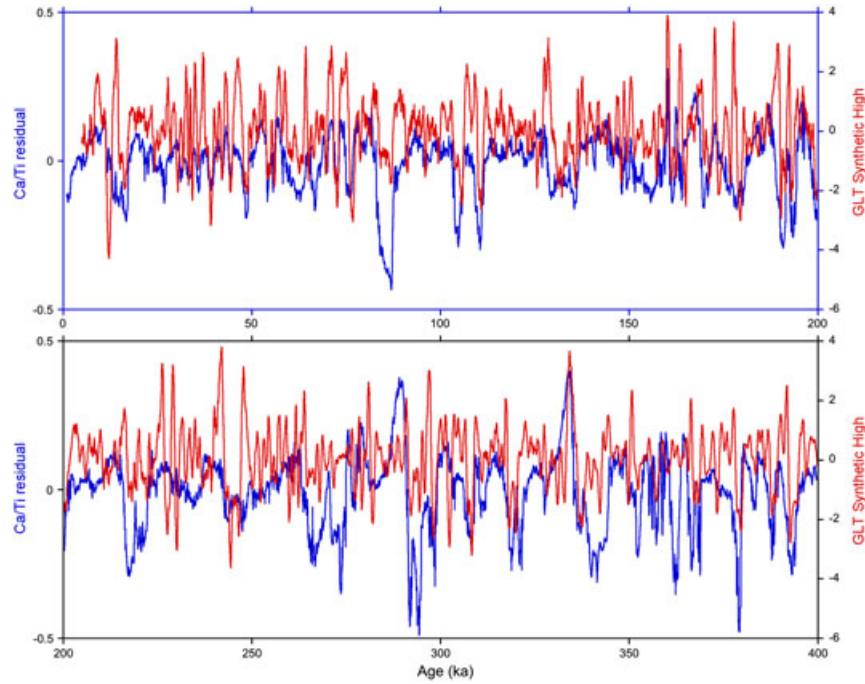
Figure 4. Comparison of Ca/Ti residual (blue) and Greenland synthetic high record (red) of *Barker et al.* [2011]. The prominent lows in Ca/Ti correspond to inferred cold stadials in the synthetic Greenland record.
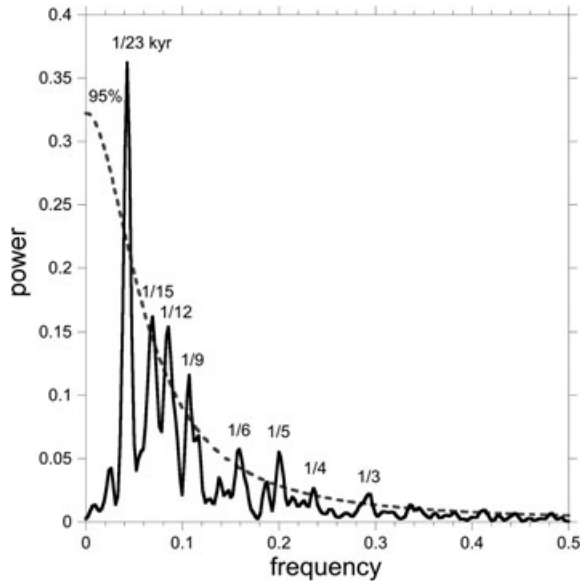
Figure 5. Multitaper method power spectrum of Ca/Ti residual using REDFIT [*Schulz and Mudelsee*, 2002]. The signal contains particularly strong power at precession (1/23 kyr) and higher frequencies.

on the continental shelf during interglacial periods [*Thomson et al.*, 1999].

[25] To further investigate the source of CaCO$_3$ variability on the Iberian margin, we measured ^{87}Sr/^{86}Sr and δ^{18}O of bulk carbonate and fine-fraction carbonate in selected samples from Core MD01-2444 (Figure 8). Significant amounts of reworking of calcareous nannoplankton have been reported in Core MD01-2444 [*Incarbona et al.*, 2010].

^{87}Sr/^{86}Sr is sensitive to reworking of older carbonate because older carbonate is likely to have a lower ^{87}Sr/^{86}Sr than late Pleistocene carbonate as the ^{87}Sr/^{86}Sr of seawater has steadily increased over the past 160 Ma [*McArthur et al.*, 2001]. Indeed, there is a significant negative correlation between ^{87}Sr/^{86}Sr and percent reworked nannofossil taxa (Figure 8a).

[26] We also measured the δ^{18}O of bulk carbonate in MD01-2444 and found that ^{87}Sr/^{86}Sr and bulk carbonate δ^{18}O are positively correlated, whereas percent reworked nannofossil taxa and bulk carbonate δ^{18}O are negatively correlated (Figure 8b). This suggests that the δ^{18}O of the reworked carbonate has lower values than biogenic carbonate. The δ^{18}O of bulk carbonate is a mirror image of the *G. bulloides* δ^{18}O record with bulk δ^{18}O decreasing during stadials when planktic δ^{18}O increases (Figure 9). *Lebreiro et al.* [2009] observed a similar relationship between planktic and bulk δ^{18}O and attributed the low bulk carbonate δ^{18}O values to land exported detrital carbonate. They also reported a higher frequency of turbidites during millennial-scale low sea-level stands, which may have increased detrital sedimentation through lateral advection.

[27] Whereas carbonate content is controlled by detrital input on glacial-interglacial time scales, we suggest it is affected by variations in carbonate productivity on millennial time scales. Low carbonate productivity is supported during stadials by low bulk carbonate δ^{18}O, high abundances of *F. profunda* (Figure 9), and cold SSTs that mark the arrival of Arctic surface waters [*Incarbona et al.*, 2010]. The relative percentage of reworked taxa increases as the background biogenic carbonate productivity diminishes.

5.2. Peaks in Ba at Terminations

[28] Similarly to *Thomson et al.* [2000], we observe peaks in Ba on terminations I–IV (Figure 6). Barium
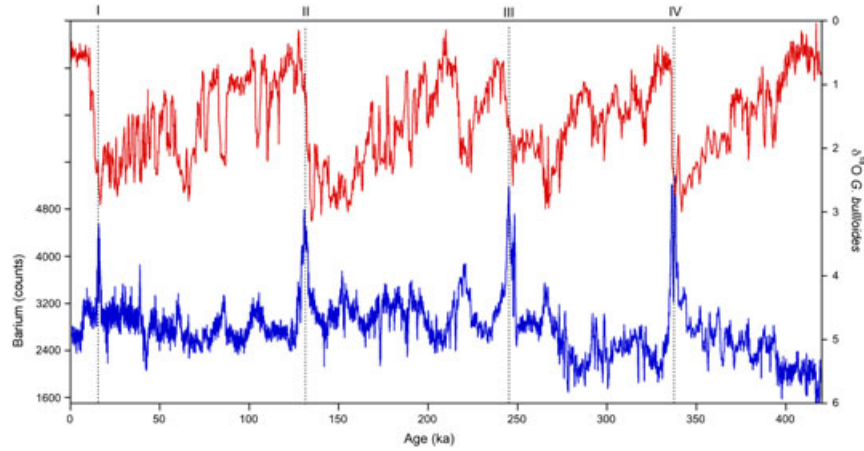
Figure 6. The XRF barium counts (blue) and $\delta^{18}O$ of *G. bulloides* (red). Vertical dashed line mark barium peaks on glacial terminations (roman numerals), which have been interpreted as indicating increased biological productivity (*Thomson et al.*, 2000).
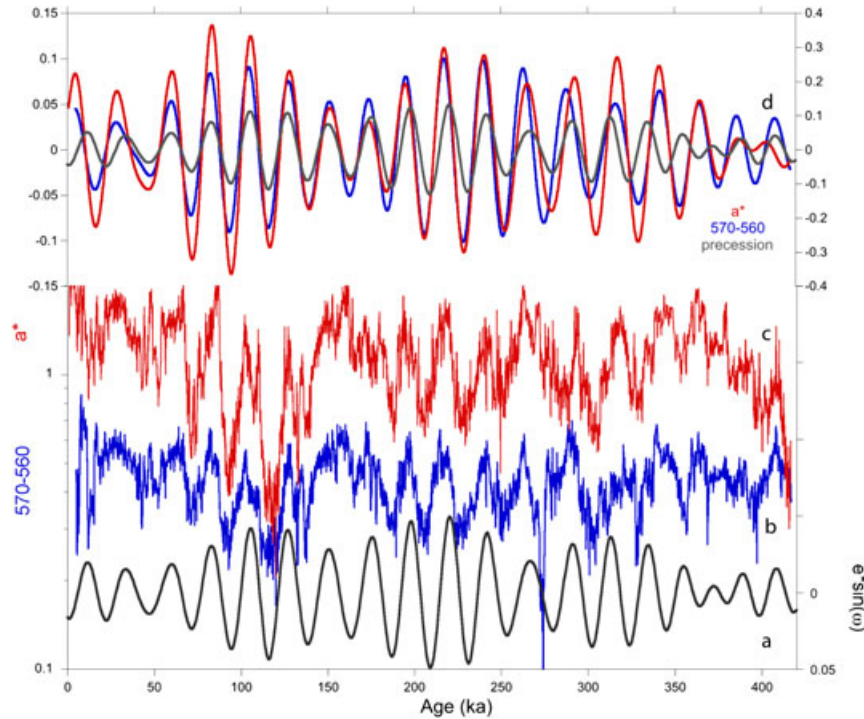
Figure 7. Comparison of the precession index (e*sinω) (a) with variations in sediment redness parameters including a* (red-green) (b) and first derivative of color reflectance at 570–560 nm, a proxy for hematite c. Top panel (d) shows bandpass filters of the a* (red) and 570–560 nm (blue) signals centered at 0.042 ± 0.01 relative to precession. The three signals are in phase with peaks in sediment redness coinciding with precession minima (i.e., peak boreal summer insolation).

concentrations in sediments have been used as a proxy of biological productivity but it can also be affected by sediment source (e.g., detrital input) and post-depositional remobilization. During sulfate reduction, sulfate concentrations in sediment pore waters are lowered and barite ($BaSO_4$) can dissolve. Sulfate reduction is not an important process in the piston cores, however, because pore-water sulfate measurements at Site U1385 remain near seawater values in the upper 40m of the sediment profile [*Stow et al.*, 2012]. Because the bases of our piston cores are less than 30 mbsf, they have not yet been through the zone of intense sulfate reduction. *Thomson et al.* [2000] ascribed the deglacial Ba peaks in Core MD95-2039 to increased productivity, which is supported by enhanced organic carbon content and diatom abundances.

5.3. Causes of Sediment Redness

[29] The proxies of sediment redness (a* and 570–560 nm) are sensitive to both changes in sediment source of Fe-rich minerals (e.g., hematite) and redox state of iron in clay minerals [*Giosan et al.*, 2002]. Color reflectance in the longer
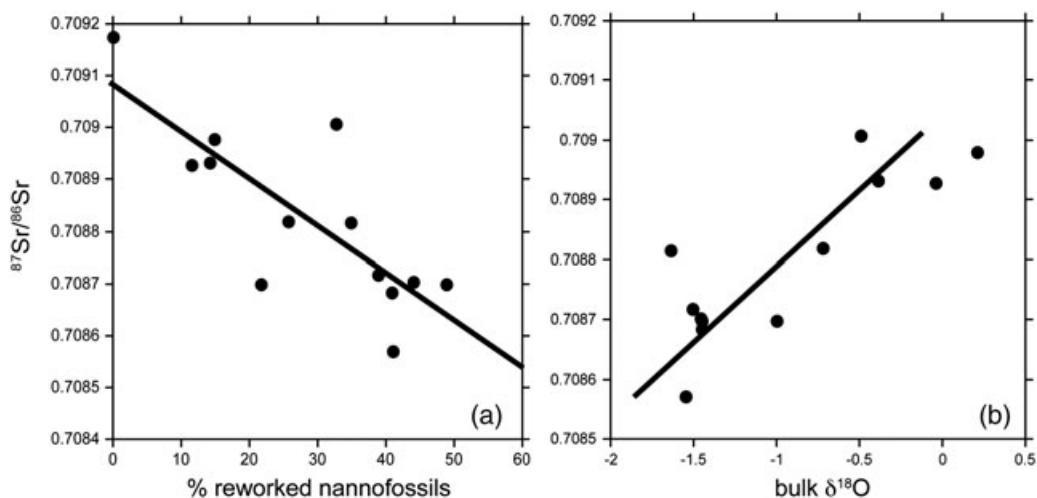
Figure 8. (a) $^{87}Sr/^{86}Sr$ of bulk carbonate versus percent reworked nannofossil taxa [*Incarbona et al.*, 2010] and (b) $^{87}Sr/^{86}Sr$ versus $\delta^{18}O$ of bulk carbonate. $^{87}Sr/^{86}Sr$ decreases with increased reworking and lower bulk $\delta^{18}O$ indicating a greater contribution of old carbonate.
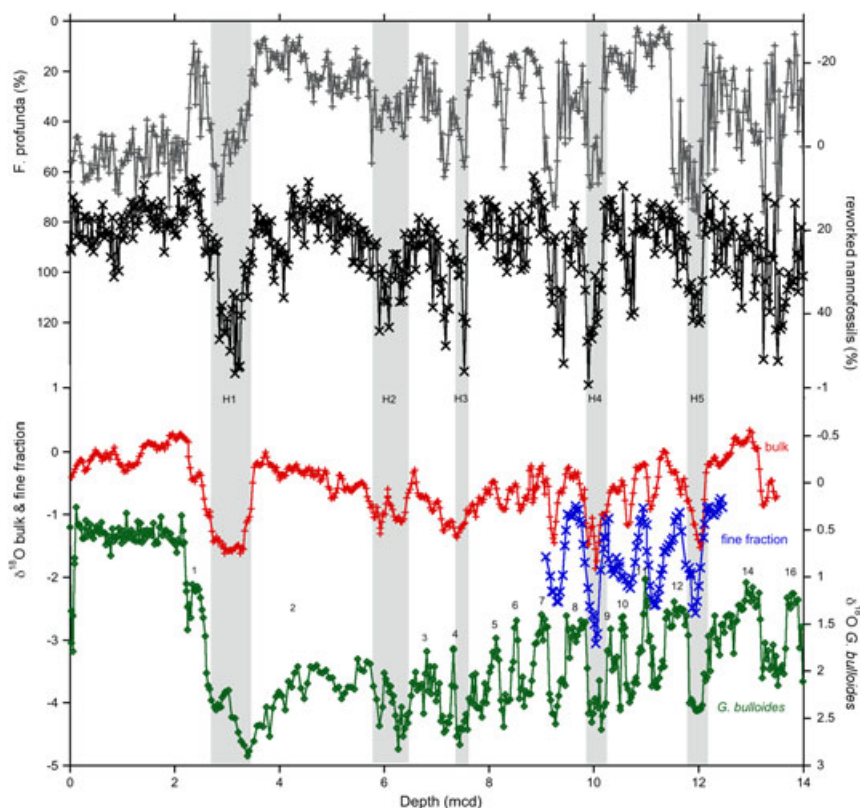
Figure 9. $\delta^{18}O$ of *G. bulloides* (green), fine-fraction $\delta^{18}O(<63m$; blue), bulk $\delta^{18}O$ (red), percent reworked nannofossil taxa (black), and percent *Florisphaera profunda* (gray) [*Incarbona et al.*, 2010] in Core MD01-2444. Heinrich stadials are marked by high planktic $\delta^{18}O$, low bulk $\delta^{18}O$, and increased reworking and abundances of *F. profunda*.

wavelengths of the visible spectrum has been used to detect iron-oxide minerals at very low concentrations. Less than 1% hematite by weight can impart a red color visible to the human eye, and concentrations as low as 0.03% have been detected in a matrix of North Atlantic sediment [*Deaton and Balsam*, 1991]. Hematite displays a characteristic peak in the first derivative of the reflectance curve at either 565 or 575 nm. The height of the peak increases as the percentage of hematite increases and the peak differential wavelength increases slightly as hematite concentration increases.

[30] Variations in a* are well correlated with changes in the first derivative of the color spectrum at 575 nm, suggesting that the primary cause of sediment redness is hematite abundance (Figure 7). This is further supported by

environmental magnetism, specifically the S-ratio, which is sensitive to the concentration of high-coercivity minerals such as hematite and/or goethite [*Robinson*, 1986; *Bloemendal et al.*, 1988, 1992; *Liu et al.*, 2007]. Both of these parameters are correlated with sediment redness (a* and 570–560 nm) with peaks in redness associated with decreases in S-ratios, which is indicative of increased hematite (see Supporting Information).

[31] We consider two potential sources of the hematite: aeolian derived from dust source areas in North Africa and/or fluvial derived from the Tagus and other river systems. Transport of African dust to the Iberian Peninsula and Gulf of Cadiz is significant today [*Negral et al.*, 2012; *Rodríguez et al.* 2001, 2002; *Escudero et al.*, 2005; *Querol et al.*, 2009; *Avila et al.*, 1997] and in the past [*Stumpf et al.*, 2010; 2011]. During summer, a thermal low develops over the North African Sahara as a result of the intense surface heating. An upper level high creates a pressure gradient that convects dust to high altitudes (3–5 km) where it is transported over a wide area of the Mediterranean, including the Gulf of Cadiz and Iberian Peninsula [*Negral et al.*, 2012; *Knippertz and Todd*, 2012].

[32] Dust flux is related to both aridity in the source region and atmospheric conditions that promote dust transport. Increases in dust deposition have been related previously to precession minima off the Moroccan coast [*Bozzano et al.*, 2002; *Moreno et al.*, 2001, 2002]. Peaks in redness in Iberian Margin cores correlate well with Fe in Core GeoB 4205 off Morocco for the last 225–250 ka (see Supporting Information). *Bozzano et al.* [2002] suggested that aridity of the source region is a necessary condition for dust availability, but storminess and turbulence are also needed to uplift dust and inject it into the troposphere. Insolation maxima associated with precession minima lead to intense surface heating and low pressure over the North African Sahara, which is favorable for carrying dust to offshore NW Africa and the Iberian Margin.

[33] At the same time, precession minima are associated with greater seasonality and intensity of the African monsoon, resulting in increased precipitation and "greening of the Sahara." The increased vegetation results in soil stabilization and decreased dust flux. Thus, the two mechanisms of increased dust transport and decreased availability in source areas compete with one another during precession minima. For the Northwest coast of Morocco, and presumably the Iberian margin, *Bozzano et al.* [2002] suggested that dust transport is the dominant of the two mechanisms. *Rogerson et al.* [2006] studied cores from the western Gulf of Cadiz and also suggested that the region receives a significant supply of aeolian detritus during summer under persistent trade winds. Hematite could also be delivered to the Iberian Margin by rivers (e.g., Tagus) because it is commonly found in soils (e.g., *Terra Rossa)* and outcrops in Portugal and Spain. Increased fluvial transport of hematite during precession minima would imply increased sediment load related to either increased precipitation and/or erosion. Modeling results suggest that runoff to the north Mediterranean increased in October-March during precession minima [*Meijer and Tuenter*, 2007]. Fluvial and aeolian delivery of hematite may also be linked in that much of the deposition of African dust in the western Mediterranean occurs as wet deposition [*Escudero et al.*, 2005]. It may be the combined effects of increased transport of dust during dry summers, and increased winter rainfall and runoff, that were responsible for the increased delivery of hematite during precession minima.

[34] Sediment redness is also affected by redox state by altering the oxidation state of iron in clay minerals [*Giosan et al.*, 2002]. Increased redness (higher a*) is associated with a more oxidizing environment, whereas sediment color tends to become greener (lower a*) with progressively more reducing conditions. Organic biomarkers have been used to estimate paleo-oxygen conditions assuming differential degradation of organic compounds under oxic and anoxic conditions. The relative proportion of n-hexacosan-1-ol ($C_{26}OH$) to the sum of $C_{26}OH$ plus n-nonacosane (C_{29}) has been proposed as a chemical proxy that reflects the oxygenation of bottom water [*Cacho et al.*, 2000; *Martrat et al.*, 2007]. The rationale is that both $C_{26}OH$ and C_{29} are derived from a common terrestrial source, but the alcohol is more susceptible to degradation under oxic conditions than the alkane. A lower ratio corresponds to increased oxidation and poorer preservation. *Martrat et al.* [2007] interpreted the alcohol ratio as a proxy for deep-water ventilation on the Iberian Margin, but the ratio is also sensitive to redox conditions in sediment pore waters [*Zonneveld et al.*, 2010], which is affected by organic matter flux to the sediment from the overlying water column.

[35] Bromine counts measured by scanning XRF have been shown to be a useful proxy for total organic carbon in marine sediment cores [*Ziegler et al.*, 2008]. Bromine and $C_{26}OH/$ ($C_{26}OH + C_{29}$) are positively correlated in MD01-2444 and -2443 except for the uppermost part of the cores (see Supporting Information), indicating better preservation of organic matter and alcohols under more reducing conditions. Bromine is anti-correlated with sediment redness (a* and 570–560 nm) suggesting less organic matter preservation when sediments are redder and more oxidized (lower alcohol ratio) (see Supporting Information). Thus, the observed sediment color variations may also be affected by changes in pore-water redox conditions, driven by changes in deep-water oxygen concentrations and/or organic carbon flux to the sediment.

[36] Sediment redness (a* and 570–560 nm) and $C_{26}OH/$ ($C_{26}OH + C_{29}$) show strong power at 19–23 kyr that is coherent and in phase with precession (Figure 10). Maximum redness and minimum alcohol ratios correlate with precession minima or boreal summer insolation maxima. The in-phase relationship of these parameters suggests a rapid response to insolation forcing, which is most likely achieved via the atmosphere. We suggest these changes are related to wind-driven processes. For example, wind-induced changes in organic export production would change organic carbon flux and redox conditions in sediment pore waters. Insolation-driven changes in winds could affect transport of African dust and delivery of hematite to Iberian Margin sediments. Regardless of the actual causal mechanisms, the fact that sediment redness and $C_{26}OH/(C_{26}OH + C_{29})$ are in phase with precession with effectively no lag provides a powerful tool that can be used for orbital tuning and assessing age models [e.g., *Shackleton et al.*, 1990]. This will be particularly important for astronomically tuning the long record obtained at IODP Site U1385.

5.4. Response to Orbital Forcing

[37] Phase relationships among co-registered proxies from the Iberian margin permit examination of the sequence of
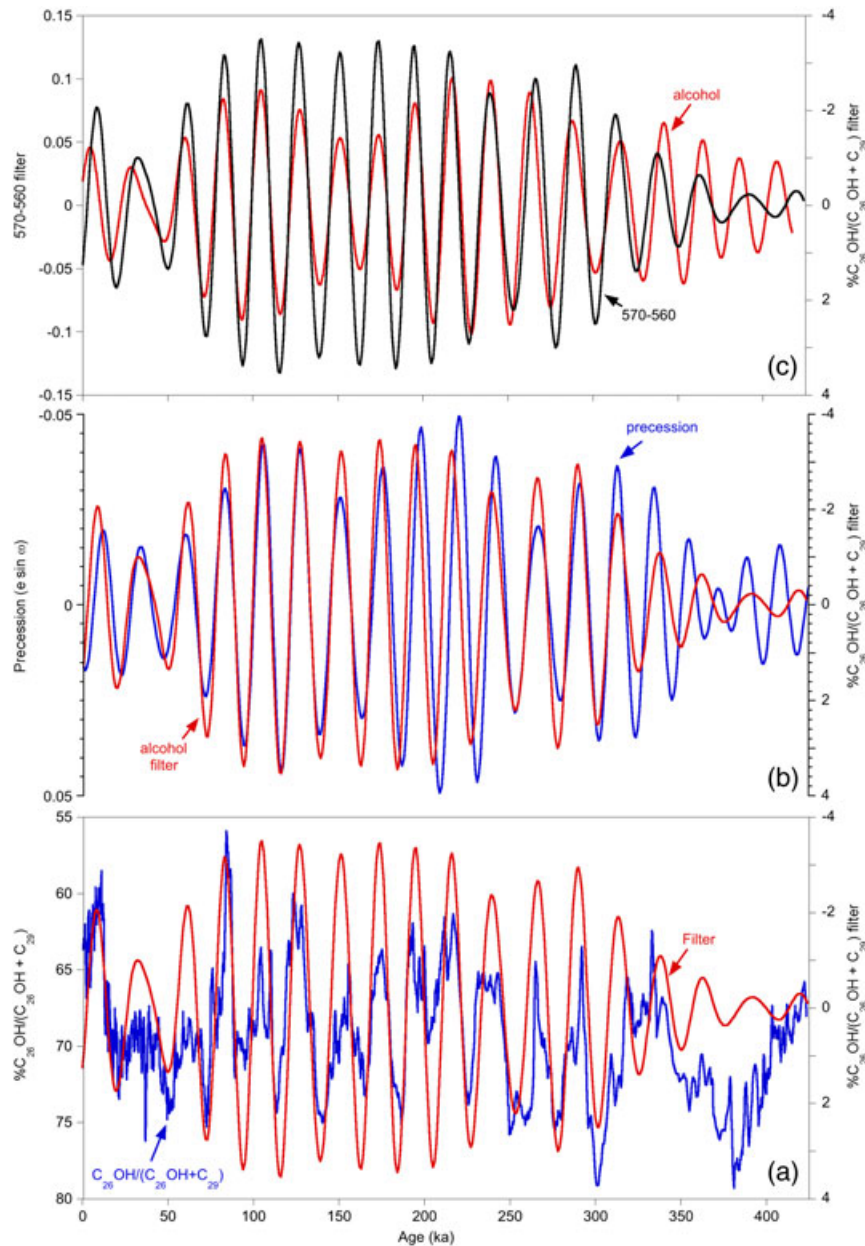
Figure 10. (a) Percent $C_{26}OH/(C_{26}OH + C_{29})$ (blue) and filtered signal centered at 0.042 ± 0.01 (red); (b) orbital precession (e*sinω) (blue) and filtered $\%C_{26}OH/(C_{26}OH + C_{29})$ signal centered at 0.042 ± 0.01 (red); and (c) filtered signals of derivative of color reflectance at 570–560 nm (blue) and $\%C_{26}OH/(C_{26}OH + C_{29})$ signal centered at 0.042 ± 0.01 (red). The alcohol index has strong 23-kyr power that is in phase with precession and sediment redness.

responses to insolation forcing, thereby providing insight into the processes by which external orbital forcing is transmitted through the climate system. With synchronization of time scales between the Iberian Margin and Antarctic ice cores using the common time scale of *Barker et al.* [2011], the phase responses of Antarctic (temperature, gases, etc.) proxies can be compared with Iberian and other marine sediment records. We placed the deconvolved benthic $\delta^{18}O$ record of Site 1123 on the same time scale to illustrate the response of deep-water temperature and $\delta^{18}O_{seawater}$, which is presumed to represent ice volume [*Elderfield et al.*, 2012]. Cross-spectral analysis was performed between each proxy time series and "ETP," which is a combination of

normalized eccentricity-tilt-precession [*Berger and Loutre*, 1999]. Because the record is only 400 kyrs long, "ETP" was modified slightly by subtracting the long 400-kyr trend in eccentricity. Coherence and phase angles are given in Table 1 and depicted on phase wheels in Figure 11. The cross-spectra for each variable relative to ETP are shown in the Supporting Information.

5.4.1. Precession
[38] Zero on the phase wheel corresponds to the precession minima when perihelion occurs at boreal summer solstice, resulting in maximum summer insolation (Figure 11a). Variations in sediment redness (a* or 570–560 nm) and $C_{26}OH/(C_{26}OH + C_{29})$ show an almost instantaneous response to

Table 1. Coherency and Phase of ice Core and Marine Sediment Parameters Relative to ETP

	Coherency	Phase angle	Phase Error	Phase (kyr)
Precession (min)				
1123 deep temp	0.96	9.9	7.6	0.6
neg($C_{26}OH/$ ($C_{26}OH + C_{29}$))	0.91	18.7	11.8	1.1
EDC temperature	0.91	22.2	11.8	1.3
570–560 nm	0.86	25.7	15.0	1.5
EDC CH_4	0.91	38.8	11.7	2.3
(neg) benthic $\delta^{18}O$	0.96	64.0	7.4	3.7
EDC CO_2	0.87	75.2	14.7	4.4
(neg) planktic $\delta^{18}O$	0.92	104.8	11.1	6.1
Ca/Ti	0.81	112.4	18.1	6.6
SST	0.93	113.8	9.8	6.6
(neg) 1123 $\delta^{18}O_w$	0.73	120.3	23.0	7.0
benthic $\delta^{13}C$	0.88	124.3	14.0	7.3
Obliquity (max)				
EDC temperature	0.97	32.8	6.1	3.7
1123 deep temp	0.80	46.3	18.5	5.3
EDC CH_4	0.88	45.0	14.0	5.1
(neg) planktic $\delta^{18}O$	0.94	58.4	9.6	6.6
(neg) benthic $\delta^{18}O$	0.93	60.7	10.3	6.9
Ca/Ti	0.76	64.0	21.3	7.3
SST	0.89	63.9	13.1	7.3
neg($C_{26}OH/$ ($C_{26}OH + C_{29}$))	0.94	65.2	9.7	7.4
(neg) 1123 $\delta^{18}O_w$	0.85	69.1	15.9	7.9
EDC CO_2	0.83	68.9	17.2	7.8
benthic $\delta^{13}C$	0.79	86.8	19.5	9.9
Eccentricity (max)				
570–560	0.64	−175.2	28.4	−48.7
a*	0.79	−168.4	19.3	−46.8
1123 deep temp	0.95	−36.8	8.5	−10.2
EDC temperature	0.92	−24.9	11.1	−6.9
neg($C_{26}OH/$ ($C_{26}OH + C_{29}$))	0.82	−19.8	17.4	−5.5
EDC CO_2	0.94	−6.8	9.7	−1.9
(neg) benthic $\delta^{18}O$	0.95	−2.7	8.0	−0.8
SST	0.94	5.5	9.4	1.5
EDC CH_4	0.91	3.8	11.6	1.1
(neg) planktic $\delta^{18}O$	0.92	12.2	10.7	3.4
(neg) 1123 $\delta^{18}O_w$	0.86	34.6	14.8	9.6
benthic $\delta^{13}C$	0.83	30.5	17.2	8.5
Ca/Ti	0.73	43.3	23.0	12.0

[40] Methane also shows a relatively early response and lags precession by ~2 kyr in agreement with other estimates [*Spahni et al.*, 2005; *Loulergue et al.*, 2008]. The precession component of the methane signal is influenced by changes in monsoon intensity and the position of the Intertropical Convergence Zone [*Loulergue et al.*, 2008; *Konijnendijk et al.*, 2011]. Indeed, pollen studies of deep-sea cores from the Iberian margin have noted the similarity between changes in Mediterranean evergreen sclerophylls and deciduous oaks and the record of atmospheric methane [*Tzedakis et al.*, 2004, 2009; *Sánchez Goñi et al.*, 2008].

[41] Negative benthic $\delta^{18}O_{calcite}$ from the Iberian Margin lags precession by 4 kyr, but the benthic $\delta^{18}O$ signal is a composite of changing temperature and $\delta^{18}O_{water}$. In turn, the $\delta^{18}O_{water}$ signal can be affected by both local hydrographic and global (ice volume) effects, with each potentially having a different phase relative to orbital forcing [*Skinner and Shackleton*, 2005, 2006]. At ODP Site 1123 in the Southwest Pacific, *Elderfield et al.* [2010; 2012] used Mg/Ca to deconvolve the benthic $\delta^{18}O_{calcite}$ signal into its temperature and $\delta^{18}O_{water}$ components, and the latter was assumed to mostly represent ice volume changes. We have plotted deep-water temperature and $\delta^{18}O_{water}$ from Site 1123 on the phase wheels to illustrate the lag between the two components. The $\delta^{18}O_{water}$ (ice volume) component at Site 1123 significantly lags precession and deep-water temperature by about 7 kyr.

[42] Atmospheric CO_2 does not respond as early to precessional insolation forcing as Antarctic temperature or methane and lags by ~4 kyr. A cluster of "late responders" lag precession by 6–7 kyr including planktic $\delta^{18}O$, SST, Ca/Ti, and benthic $\delta^{13}C$ from the Iberian Margin. These parameters have nearly the same phase as the $\delta^{18}O_{water}$ (ice volume) component of the Pacific benthic $\delta^{18}O_{calcite}$ signal and may be related to high-latitude changes in continental ice sheets. Northern Hemisphere ice sheets exert a strong downstream control on climate variables in the North Atlantic such as the position of the polar front, sea ice, and formation of deep water.
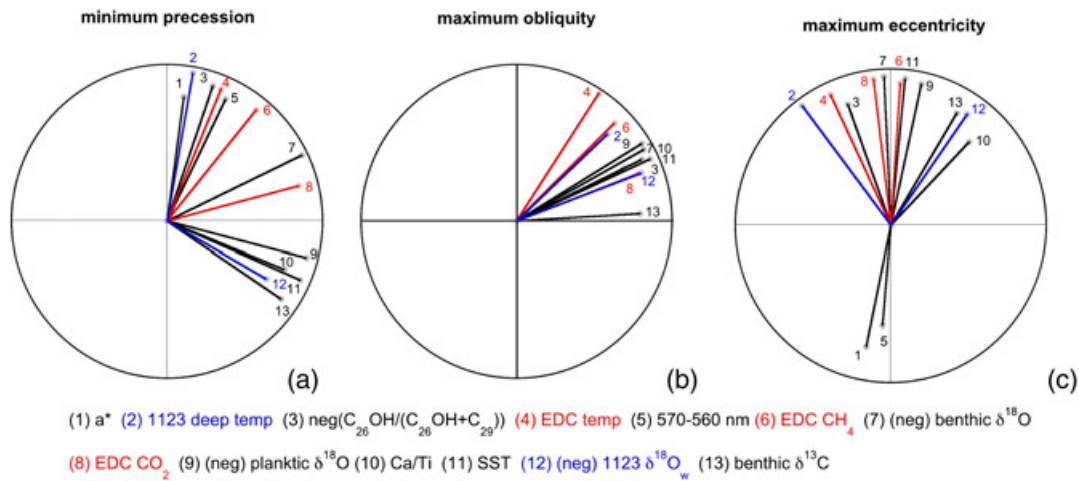
5.4.2. Obliquity

[43] Zero on the phase wheel corresponds to the maximum obliquity (Figure 11b). There is no significant power at obliquity in either of the redness proxies (a* and 570–560 nm). This argues in favor of a low-latitude response to insolation forcing because the effects of obliquity on low-latitude insolation are small in comparison to those of precession. In contrast to sediment redness, the $C_{26}OH/(C_{26}OH + C_{29})$ ratio has significant power at 41 kyr that lags obliquity by 8 kyr. Most other Iberian margin sediment parameters also lag obliquity maxima by 7 to 8 ka, including Ca/Ti, planktic and benthic $\delta^{18}O$, and SST. Benthic $\delta^{13}C$ lags maximum obliquity by 10 kyr. Antarctic temperature and atmospheric methane lag by 1–2 kyr, whereas CO_2 and ice volume ($\delta^{18}O_{water}$) lag by 8 kyr.

[44] The observed phase relationships support *Ruddiman's* [2003, 2006] suggestion that, unlike the precession cycle where CO_2 leads ice volume, CO_2 has the same late response as $\delta^{18}O_{water}$ in the obliquity band. Whereas the early CO_2 response forces ice volume changes in the precession band, the late response in the obliquity band acts more as a feedback.

5.4.3. Eccentricity

[45] Zero on the phase wheel corresponds to maximum eccentricity (Figure 11c). Phase relationships at eccentricity must be interpreted with caution because of the short

precessional insolation forcing with a negligible lag (<1 kyr), with peaks in redness and lows in $C_{26}OH/(C_{26}OH + C_{29})$ occurring near precession minima (summer insolation maxima). The rapid in-phase response of these proxies supports our interpretation of an atmospheric link, such as winds inducing changes in dust transport, precipitation, and/or upwelling.

[39] Sediment redness (a* or 570–560 nm) and $C_{26}OH/(C_{26}OH + C_{29})$ are also in phase with Antarctic temperature. Maxima in Antarctic temperature occur at precessional minima [*Kawamura et al.*, 2007; *Jouzel et al.*, 2007], which is unexpected given this orbital configuration coincides with a minimum in austral summer insolation. *Laepple et al.* [2011] suggested the δD signal in Antarctic ice cores may indeed be biased toward austral winter because of a seasonal cycle in snow accumulation. Alternatively, *Huybers and Denton* [2008] noted that precession minima are associated with increased length of the austral summer. They proposed the high-latitude Northern Hemisphere responds to local summer intensity, whereas the polar regions of the Southern Hemisphere respond to local summer duration.

Figure 11. Phase wheels for proxy records with respect to (a) minimum precession, (b) maximum obliquity, and (c) maximum eccentricity. The length of the vector is the coherency from 0 (center) to 1 (circle). Numerical values of coherency and phase values are given in Table 1. Iberian Margin proxies are black, ice cores are blue, and Site 1123 is red. The signs of oxygen isotopes records and alcohol index are inverted.

length of the records (420 kyr) [*Ruddiman*, 2003]. At the 100 kyr eccentricity cycle, Antarctic temperature and deep-water temperature in the SW Pacific lead eccentricity maxima by 6 kyr, whereas CO_2, CH_4, and Iberian SST are nearly in phase with eccentricity. This is consistent with findings of *Shackleton* [2000] who reported Antarctic and deep-water temperature leads eccentricity by 5 kyr, whereas CO_2 is in phase with eccentricity within error. *Ruddiman et al.* [2003] suggested the early lead of Southern Ocean temperature is an artifact of signal rectification, but *Elderfield et al.* [2012] argued that the phase relationship could be due to a differential lag of climate response to warm season duration (inverse eccentricity) versus insolation intensity (conventional eccentricity). Although this may explain the phase relationship in theory, no specific mechanism was proffered, while the association between the apparent phase lag and the expansion of ice sheets at the mid-Pleistocene transition suggests that ice sheet behavior is implicated.

[46] A number of Iberian margin proxies are 180° out of phase with respect to eccentricity maxima (Figure 11c). Whereas sediment redness proxies (a* and 570–560 nm) are in phase with precession, they are out of phase with respect to eccentricity with redder sediments occurring during eccentricity minima. Similarly, negative benthic and planktic $\delta^{18}O$ are in phase with maximum eccentricity, which is equivalent to the $\delta^{18}O$ maxima coinciding with eccentricity minima. This phase relationship between the 100 kyr power of eccentricity and benthic $\delta^{18}O$ has been noted previously [*Hays et al.*, 1976; *Berger et al.*, 2005].

[47] The phases of the redness proxies and CH_2O_6/ $(CH_{2}O_{6-} + C_{29})$ are different for eccentricity than for precession. The alcohol ratio is in phase with Antarctic temperature and leads eccentricity, whereas the redness proxies are out of phase. Minima in the alcohol ratio (increased oxygenation) have the same phase as Antarctic temperature and lead eccentricity maxima, whereas sediment redness is out of phase and greatest near eccentricity minima. This opposite phasing suggests a fundamentally different response of these proxies at the 100 kyr cycle than observed for precession. One

plausible explanation for this decoupling is sediment redness is controlled by both source of hematite and redox state in sediment pore waters, whereas the alcohol ratio is dependent mainly on sediment redox conditions. An increase in hematite delivery to sediments that are reduced will still make them red. For example, more intense winds and aridity in dust source areas may have resulted in increased transport of hematite to the Iberian Margin and, at the same time, more reducing conditions in sediment pore waters related to upwelling and organic carbon export. This explanation is not unique but rather serves as an example of how a different phase response could be recorded by these proxies at precession and eccentricity frequencies.

[48] The phase vector of benthic $\delta^{18}O_{calcite}$ reflects a combination of changes in temperature and $\delta^{18}O_{water}$. The latter is affected by both hydrography and ice volume on the Iberian Margin [*Skinner and Shackleton*, 2005, 2006; *Skinner et al.*, 2007]. At Site 1123 in the SW Pacific, the deconvolved benthic $\delta^{18}O$ signal indicates that the ice volume component lags Antarctic and deep-water temperature by 20 kyr at 100-kyr periodicities, equivalent to a full precession cycle [*Elderfield et al.*, 2012]. Ice volume minima (i.e., negative $\delta^{18}O_{water}$ at Site 1123) lags eccentricity maxima by 10 kyr, which is similar to 14 kyr estimate of *Shackleton* [2000] derived independently using $\delta^{18}O$ of atmospheric O_2 to separate the ice volume component of benthic $\delta^{18}O$. Ice volume ($\delta^{18}O_{water}$) similarly lags CO_2 by 10 kyr, which led *Shackleton* [2000] to conclude that the 100 kyr cycle cannot arise from ice sheet dynamics, but instead may be related to the response of the global carbon cycle. *Ruddiman* [2003, 2006] disagreed arguing that CO_2 had a phase closer to that of eccentricity, and the lag of benthic $\delta^{18}O_{water}$ (assumed to represent ice volume) was no more than 5000 years. The deconvolved $\delta^{18}O$ signal from Site 1123 suggests otherwise [*Elderfield et al.*, 2012]; thus, CO_2 may yet play an important role in generation of the 100 kyr cycle [*Shackleton*, 2000].

5.5. Caveats

[49] It is important to note the phasing we describe here applies to orbital timescales. We have ignored other sources

of variation acting at frequencies greater than a precession cycle and have not considered potential interactions of climate variability on millennial and orbital timescales. In principle, introduction of millennial scale variability could affect the phase at orbital time scales with a greater impact for the 100 kyr cycle than for higher frequencies. *Alley et al.* [1989] pointed out the bipolar seesaw on millennial timescales can complicate the inference of phasing at orbital frequencies, making it difficult to determine which part of the climate system actually leads or lags. For example, Heinrich events on terminations may delay warming in the North Atlantic and advance it in the south. In general, spectral analysis should reflect an approximation of the whole wave form at a given period, but it might be affected by non-random millennial events such as those that regularly occur on glacial terminations (especially for the 100 kyr cycle).

[50] The benthic $\delta^{18}O$ signal deconvolved into its temperature and $\delta^{18}O_{water}$ components provides a much better proxy for global ice volume than stacked $\delta^{18}O$ records [*Shackleton*, 2000; *Elderfield et al.*, 2012], but $\delta^{18}O_{water}$ is also not a direct measure of ice volume. The $\delta^{18}O$ of seawater is expected to lag ice volume and sea level because the $\delta^{18}O$ of ice changes as the ice sheet grows from low elevation to high elevation [*Mix and Ruddiman*, 1984]. The $\delta^{18}O_{water}$ from the Iberian Margin will have a different phase from that of the SW Pacific because of the long oceanic transit time of the $\delta^{18}O_{water}$ signal from the North Atlantic to the deep Pacific [*Skinner and Shackleton*, 2005; *Lisiecki and Raymo*, 2009; *Gebbie*, 2012; *Friedrich and Timmermann*, 2012]. Furthermore, the $\delta^{18}O_{water}$ from the deep Iberian Margin will have a greater hydrographic contribution than the deep SW Pacific owing to the glacial-interglacial changes in northern and southern-sourced water masses [*Skinner and Shackleton*, 2005, 2006; *Skinner et al.*, 2007]. Thus, the phasing inferred for $\delta^{18}O_{water}$ from the SW Pacific does not necessarily apply to the Iberian Margin.

[51] Benthic $\delta^{13}C$ consistently shows a late response in all orbital bands (Figure 11). Similar to $\delta^{18}O$, however, the benthic $\delta^{13}C$ signal is complex because it is affected by multiple processes with each potentially having a different phase relative to orbital forcing (e.g., nutrients, gas exchange, deep-water circulation, and whole-ocean reservoir effects).

6. Conclusions

[52] Sediment geochemical and color variations in piston cores from the southwestern Iberian Margin are highly responsive to climate change on both millennial and orbital time scales. Variations in Ca/Ti are highly correlated with weight % $CaCO_3$ and reflect changing mixing ratios of biogenic (Ca) and detrital (Ti) sediment. On orbital timescales, Ca/Ti lags precession and sediment redness by ~7 kyr and is controlled mainly by variable dilution of biogenic carbonate by clays in response to changing sea level. On millennial timescales, Ca/Ti mirrors variations in planktic $\delta^{18}O$ and alkenone SST, with Ca/Ti lows corresponding to cold events (stadials). For the last glacial period, Ca/Ti resembles in great detail the Greenland ice core $\delta^{18}O$ record, capturing most of the Dansgaard-Oeschger events. The strong correlation between Ca/Ti and Greenland temperature demonstrates the potential use of this ratio at Site U1385 for documenting suborbital variability in older glacial periods and determining how it evolved

as ice volume and boundary conditions changed through the Pleistocene.

[53] Iberian Margin sediments contain very strong precession signals, which provide powerful tools for constructing and testing age models [*Shackleton*, 2000; *Shackleton et al.*, 1990]. Especially notable are the highly coherent and in-phase behavior of sediment redness proxies (a* and 570–560 nm) and $C_{26}OH/(C_{26}OH+C_{29})$) with precession. Redder sediments and more oxidizing conditions (low alcohol ratio) occur at precession minima (summer insolation maxima) with little to no phase lag. This fast response suggests these proxies are responding to low-latitude wind-driven processes (e.g., dust transport, upwelling, precipitation).

[54] A peak in the first derivative of the color spectrum at 575 nm (570–560 nm) and rock magnetic properties (S-ratio) indicate that hematite is the dominant mineral responsible for the red color. We suggest the source of the hematite is aeolian dust from Africa, although we cannot rule out fluvial input. Sediment redness depends upon both variations in source (hematite) and also redox state of the sediment. Redness is well correlated with the alcohol preservation ratio $(C_{26}OH/(C_{26}OH+C_{29}))$, indicating increased redness and oxygenation of sediment pore waters at times of precession minima, which could be related to either improved ventilation of deep water or reduced fluxes of organic carbon to the sediment.

[55] The age model was developed by synchronizing the Iberian Margin sediment record to Antarctic ice cores and speleothems on millennial timescales. This chronology is independent of oxygen isotope stratigraphy and permits new spectral estimates to be made of the phase responses to orbital forcing. Responses to precession can be divided into a group of early and late responders (i.e., following *Imbrie et al.* [1992, 1993]). Sediment redness parameters (a* and 570–560) and alcohol ratios are first to respond along with methane and Antarctic temperature (Figure 11a). Sediment redness and methane represent rapid responses to low-latitude insolation forcing whereas Antarctic temperature may be related to austral winter insolation [*Laepple et al.*, 2011], integrated summer insolation [*Huybers and Denton*, 2008], or to boreal summer insolation forcing as assumed previously. Atmospheric CO_2 shows an intermediate response, lagging precession by 4 kyr. A series of late responders lag precession by 6 or 7 kyr, including planktic $\delta^{18}O$, SST, Ca/Ti, and benthic $\delta^{13}C$, and may be associated with changes in Northern Hemisphere ice sheets.

[56] At 41 kyr periodicities, the phases of most parameters are tightly clustered, lagging obliquity maxima by 7–8 kyr. The lack of power at obliquity frequencies in sediment redness parameters supports a low-latitude forcing for this proxy.

[57] Although the lengths of the time series are short (420 ka) for detecting 100 kyr eccentricity cycles, the phase relationships support those obtained by *Shackleton* [2000]. Antarctic temperature, south Pacific deep-water temperature, and Iberian Margin alcohol ratios lead eccentricity maxima by 6 kyr [*Elderfield et al.*, 2012]. CO_2, CH_4, and Iberian SST are nearly in phase with eccentricity, and minimum ice volume (as inferred from Pacific $\delta^{18}O_{seawater}$) lags eccentricity maxima by 14 kyr. Sediment redness proxies are out of phase with eccentricity such that increased redness occurs near times of greater ice volume associated with eccentricity minima. The new phase estimates derived in this study

continue to support a potential role for the Earth's carbon cycle in contributing to the 100 kyr cycle, as originally proposed by *Shackleton* [2000].

References

Alley, R. B., E. J. Brook, and S. Anandakrishnan (1989), A northern lead in the orbital band: North–south phasing of Ice-Age events, *Quaternary Sci. Rev.*, 21, 431–441.

Avila, A., I. Queralt-Mitjans, and M. Alarcon (1997), Mineralogical composition of African dust delivered by red rains over northeastern Spain, *J. Geophys. Res.*, 102, 21977–21996.

Barker, S., G. Knorr, R. L. Edwards, F. Rarrenin, A. E. Putnam, L. C. Skinner, E. Wolff, and M. Ziegler (2011), 800,000 years of abrupt climate variability, *Science*, 334, 347–351.

Barranco, F. T., Jr., W. L. Balsam, and B. C. Deaton, (1989), Quantitative reassessment of brick red lutites: evidence from reflectance spectrophotometry, *Mar. Geol.*, 89, 299–314.

Berger, A., and M. F. Loutre (1999), Parameters of the Earth's orbit for the last 5 million years in 1 kyr resolution. doi:10.1594/PANGAEA.56040.

Berger, A., J. L. Mélice, and M. F. Loutre (2005), On the origin of the 100-kyr cycles in the astronomical forcing, *Paleoceanography*, 20, PA4019, doi:10.1029/2005PA001173.

Bloemendal, J., B. Lamb, and J. W. King, (1988), Paleoenvironmental implications of rock-magnetic properties of Late Quaternary sediment cores from the eastern equatorial Atlantic, *Paleoceanography*, 3, 61–87.

Bloemendal, J., J. W. King, F. R. Hall, and S. J. Doh (1992), Rock magnetism of Late Neogene and Pleistocene deep-sea sediments: Relationship to sediment source, diagenetic processes, and sediment lithology. *J. Geophys. Res.* 97, 4361–4375.

Bozzano, G., H. Kuhlmann, and B. Alonso (2002), Storminess control over African dust input to the Moroccan Atlantic margin (NWAfrica) at the time of maxima boreal summer insolation: A record of the last 220 kyr, *Palaeogeogr. Palaeoclimatol. Palaeoecol.*, 183, 155–168.

Cacho, I., J. O. Grimalt, M. Canals, L. Sbaffi, N. J. Shackleton, J. Schonfeld, and R. Zahn, (2000), Variability of the western Mediterranean Sea surface temperature during the last 25,000 years and its connection with the Northern Hemisphere climatic changes, *Paleoceanography*, 16, 40–52.

de Abreu, L., F. G. Abrantes, N. J. Shackleton, P. C. Tzedakis, J. F. McManus, D. W. Oppo, and M. A. Hall (2005), Ocean climate variability in the eastern North Atlantic during interglacial marine isotope stage 11: A partial analogue to the Holocene?, *Paleoceanography*, 20, PA3009, doi:10.1029/2004PA001091.

Deaton, B. C., and W. L. Balsam (1991), Visible spectroscopy: A rapid method for determining hematite and goethite concentration in geological materials, *J. Sediment. Petrol.*, 61, 628–632.

Elderfield, H., P. Ferretti, M. Greaves, S. Crowhurst, I. N. McCave, D. A. Hodell, and A. M. Piotrowski (2012), Evolution of ocean temperature and ice volume through the Mid-Pleistocene climate transition, *Science*, 337, 704–709.

Elderfield, H., M. Greaves, S. Barker, I. Hall, A. Tripati, P. Ferretti, L. Booth, and C. Daunt (2010), A record of bottom water temperature and seawater δ18O for the Southern Ocean over the past 440 kyr based on Mg/Ca of benthic foraminiferal *Uvigerina* spp., *Quaternary Sci. Rev.*, 29, 160–169.

Escudero, M., S. Castillo, X. Querol, A. Avila, M. Alarcón, M. M. Viana, A. Alastuey, E. Cuevas, and S. Rodríguez (2005), Wet and dry African dust episodes over Eastern Spain, *J. Geophys. Res.*, 110, D18S08.

Expedition 339 Scientists (2012), Mediterranean outflow: environmental significance of the Mediterranean Outflow Water and its global implications, *IODP Prel. Rept.*, 339, doi:10.2204/iodp.pr.339.2012.

Friedrich, T., and A. Timmermann (2012), Millennial-scale glacial meltwater pulses and their effect on the spatiotemporal benthic δ18O variability, *Paleoceanography*, 27, PA3215, doi:10.1029/2012PA002330.

Gebbie, G. (2012), Tracer transport timescales and the observed Atlantic-Pacific lag in the timing of the last termination, *Paleoceanography*, doi:10.1029/2011PA002273, in press.

Giosan, L., R. D. Flood, and R. C. Aller (2002), Paleoceanographic significance of sediment color on western North Atlantic drifts: I. Origin of color. *Mar. Geol.*, 189, 25–41.

Hays, J. D., J. Imbrie, and N. J. Shackleton (1976), Variations in the Earth's orbit: Pacemaker of the Ice Ages, *Science*, 194, 1121–1132.

Heslop, D. (2009), On the statistical analysis of the rock magnetic S-ratio. *Geophys. J. Int.*, 178, 159–161.

Howell, P., N. Pisias, J. Ballance, J. Baughman, and L. Ochs (2006), ARAND Time-Series Analysis Software, Brown University, Providence RI.

Huybers, P. (2006). Glacial variability over the last two million years: An extended depth-derived age model, continuous obliquity pacing, and the Pleistocene progression, *Quaternary Sci. Rev.*, 26, 37–55.

Huybers, P. and G. Denton (2008), Antarctic temperature at orbital time scales controlled by local summer duration, *Nature Geoscience*, 1, 787–792.

Imbrie, J., et al. (1984), The orbital theory of Pleistocene climate: Support from a revised chronology of the marine δ18O record. In: Berger, A.L., et al. (Eds.), Milankovitch and Climate, Part I. D. Reidel Publ, Dordrecht, pp. 269–305.

Imbrie, J., and J. Z. Imbrie, (1980), Modeling the climatic response to orbital variations, *Science*, 207, 943–953.

Imbrie, J., et al. (1992), On the structure and origin of major glaciation cycles: I. Linear responses to Milankovitch forcing, *Paleoceanography*, 7, 701–738.

Imbrie, J., et al. (1993), On the structure and origin of major glaciation cycles. II: The 100,000-year cycle, *Paleoceanography*, 8, 699–735.

Incarbona, A., B. Martrat, E. Di Stefano, J. O. Grimalt, N. Pelosi, B. Patti, and G. Tranchida (2010), Primary productivity variability on the Atlantic Iberian Margin over the last 70,000 years: Evidence from coccolithophores and fossil organic compounds, *Paleoceanography*, 25(2), PA2218, doi: 10.1029/2008pa001709.

Jouzel, J., et al. (2007). Orbital and millennial Antarctic climate variability over the past 800,000 years. *Science* 317, 793–796.

Kamenov, G. D., M. Brenner, and J. L. Tucker (2009), Anthropogenic vs natural control on trace element and Sr-Nd-Pb isotope record in peat sediments of southeast Florida, *USA, Geochimica et Cosmochimica Acta*, 73, 3549–3567.

Kawamura, K., , et al. (2007), Northern Hemisphere forcing of climatic cycles in Antarctica over the past 360,000 years, *Nature*, 448, 912–916.

Knippertz, P., and M. C. Todd (2012), Mineral dust aerosols over the Sahara: Meteorological controls on emission and transport and implications for modeling, *Rev. Geophys.*, 50, RG1007, doi:10.1029/2011RG000362.

Konijnendijk, T. Y. M., S. L. Weber, E. Tuenter, and M. van Weele (2011), Methane variations on orbital timescales: A transient modeling experiment, *Climate of the Past*, 7, 635–648.

Laepple, T., M. Werner, and G. Lohmann (2011), Synchronicity of Antarctic temperatures and local solar insolation on orbital timescales, *Nature*, 471, 91–94.

Lebreiro, S. M., A. H. L. Voelker, A. Vizcaino, F. G. Abrantes, U. Alt-Epping, S. Jung, N. Thouveny, and E. Gracia (2009), Sediment instability on the Portuguese continental margin under abrupt glacial climate changes (last 60 kyr), *Quaternary Sci. Rev.*, 28, 3211–3223.

Lisiecki, L. E., and M. E. Raymo (2009), Diachronous benthic δ18O responses during late Pleistocene terminations, *Paleoceanography* 24, PA3210, doi:10.1029/2009PA001732

Lisiecki, L. E., and M. E. Raymo (2005), A Pliocene-Pleistocene stack of 57 globally distributed benthic δ18O records, *Paleoceanography*, 20, PA1003, doi:10.1029/2004PA001071.

Liu, Q., A. P. Roberts, J. Torrent, C.-S. Horng, and J. C. Larrasoana (2007), What do the HIRM and S-ratio really measure in environmental magnetism?, *Geochem. Geophys. Geosyst.*, 8, Q09011, doi:10.1029/2007GC001717.

Loulergue, L., A. Schilt, R. Spahni, V. Masson-Delmotte, T. Blunier, B. Lemieux, J.- M. Barnola, D. Raynaud, T. F. Stocker, and J. Chappellaz (2008), Orbital and millennial-scale features of atmospheric CH4 over the past 800,000 years, *Nature*, 453, 383–386.

Margari, V., L. C. Skinner, P. C. Tzedakis, A. Ganopolski, M. Vautravers, and N. J. Shackleton (2010), The nature of millennial-scale climate variability during the past two glacial periods, *Nature Geoscience*, 3, 127–131.

Martrat, B., J. O. Grimalt, N. J. Shackleton, L. de Abreu, M. A. Hutterli, and T. F. Stocker (2007), Four climate cycles of recurring deep and surface water destabilizations on the Iberian margin, *Science*, 317, 502–507.

McArthur, J. M., R. J. Howarth, and T. R. Bailey (2001), Strontium isotope stratigraphy: LOWESS Version 3: Best fit to the marine Sr-isotope curve for 0–509 Ma and accompanying look-up table for deriving numerical age, *J. Geol.*, 109, 155–170.

Meijer, P.Th., and E. Tuenter (2007), The effect of precession-induced changes in the Mediterranean freshwater budget on circulation at shallow and intermediate depth, *Journal Marine Systems 68*, 349–365.

Milankovitch, M. (1941), Kanon der Erdbestrahlung und seine Andwendung auf das Eiszeitenproblem. Royal Serbian Academy Special Publication 133, Belgrade, 633pp.

Mix, A. C., and W. F. Ruddiman, (1984), Oxygen-isotope analyses and Pleistocene ice volumes, *Quaternary Res.*, 21, 1–20.

Moreno, A., Cacho, I., Canals, M., Prins, M.A., Sánchez-Goñi, M.F., Grimalt, J.O., Weltje, G.J. (2002), Saharan dust transport and high

latitude glacial climatic variability: The Alboran Sea record, *Quaternary Res.*, *58*, 318–328.

Moreno, A., J. Targarona, J. Henderiks, M. Canals, T. Freudenthal, and H. Meggers (2001), Orbital forcing of dust supply to the North Canary Basin over the last 250 kyr, *Quaternary Sci. Rev.*, *20*, 1327–1339.

Negral, L., S. Moreno-Grau, X. Querol, J. Moreno, M. Viana, A. García-Sánchez, A. Alastuey, and J. Moreno-Clavel (2012), Weak pressure gradient over the Iberian Peninsula and African dust outbreaks: A new dust long transport scenario, *B. Am. Meteorol. Soc.*, doi: 10.1175/BAMS-D-10-05000, 1125-1132.

Pin, C. and C. Bassin (1992), Evaluation of a strontium-specific extraction chromatographic method for isotopic analysis in geological materials, *Anal. Chim. Acta*, *269*, 249–255.

Querol, X., et al. (2009), African dust contributions to mean ambient PM10 mass-levels across the Mediterranean Basin, *Atmos. Environ.*, *43*, 4266–4277.

Raymo, M. E. and P. Huybers (2008), Unlocking the mysteries of the ice ages, *Nature*, *451*, 284285.

Richter, T. O. and van der Gaast, S. (2006), The Avaatech Core Scanner: Technical description and applications to NE Atlantic sediments. In: Rothwell, R.G. (Ed.), New Ways of Looking at Sediment Core and Core Data. Geological Society Special Publication, London, pp. 39–50.

Robinson, S.G. (1986), The late Pleistocene palaeoclimatic record of North Atlantic deep-sea sediments revealed by mineral-magnetic measurements. *Phys. Earth Planet. Int.*, *42*, 22–47.

Rodríguez, S., X. Querol, A. Alastuey, G. Kallos, and O. Kakaliagou (2001), Saharan dust contributions to PM10 and TSP levels in Southern and Eastern Spain, *Atmos. Environ.*, *35*, 2433–2447.

Rodríguez, S., X. Querol, A. Alastuey, and E. Mantilla (2002), Origin of high summer PM10 and TSP concentrations at rural sites in Eastern Spain, *Atmos. Environ.*, *36*, 3101–3112.

Rogerson, M., P. P. E. Weaver, E. J. Rohling, L. J. Lourens, J. W. Murray, and A. Hayes, (2006), Colour logging as a tool in high-resolution palaeoceanography, in New Ways of Looking at Sediment Cores and Core Data, R.G. Rothwell, Editor, Geological Society Special Publications: London. pp. 99–112.

Ruddiman, W.F. (2006), Orbital changes and climate, *Quaternary Sci. Rev.*, *25*, 3092–3112.

Ruddiman, W.F. (2003), Orbital insolation, ice volume, and greenhouse gases, *Quaternary Sci. Rev.*, *22*, 1597–1629.

Sánchez Goñi, M. F., A. Landais, W. J. Fletcher, F. Naughton, S. Desprat, and J. Duprat (2008), Contrasting impacts of Dansgaard-Oeschger events over a western European latitudinal transect modulated by orbital parameters, *Quaternary Sci. Rev.*, *27*, 1136–1151.

Schulz M, and M. Mudelsee (2002), REDFIT: Estimating red-noise spectra directly from unevenly spaced paleoclimatic time series, *Computers and Geosciences*, *28*, 421–426.

Shackleton, N.J. (2000), The 100,000-year ice-age cycle identified and found to lag temperature, carbon dioxide, and orbital eccentricity, *Science*, *289*, 1897–1902.

Shackleton, N. J., R. G. Fairbanks, T.-C. Chiu, and F. Parrenin (2004), Absolute calibration of the Greenland time scale: Implications for Antarctic time scales and for Δ^{14}C, *Quat. Sci. Rev.*, *23*, 1513–1522.

Shackleton, N.J., Chapman, M., Sánchez-Goñi, M.F., Pailler, D., Lancelot, Y. (2002), The classic marine isotope substage 5e, *Quaternary Res.*, *58*, 14–16.

Shackleton, N. J., M. A. Hall, and E. Vincent (2000), Phase relationships between millennial-scale events 64,000–24,000 years ago, *Paleoceanography*, *15*, 565–569.

Shackleton, N. J., A. Berger, and W. R. Peltier (1990), An alternative astronomical calibration of the lower Pleistocene timescale based on ODP Site 677, *Trans. R. Soc. Edinburgh, Earth Sci.*, *81*, 251–261.

Skinner, L. C., H. Elderfield, and M. Hall (2007), Phasing of millennial events and Northeast Atlantic deep-water temperature change since ~50 ka BP. In Schmittner, A., Chiang, J. and Hemming, S.R. (Eds.), Ocean Circulation: Mechanisms and Impacts, *AGU Geophys. Monograph*, *173*, AGU, Washington, D. C., 197–208.

Skinner, L.C., and N.J. Shackleton (2006), Deconstructing terminations I and II: Revisiting the glacioeustatic paradigm based on deepwater temperature estimates, *Quaternary Sci. Rev.*, *25*, 3312–3321.

Skinner, L.C., and N.J. Shackleton, (2005), An Atlantic lead over Pacific deepwater change across termination I: Implications for the application of the marine isotope stage stratigraphy, *Quaternary Sci. Rev.*, *24*, 571–580.

Spahni, R., et al. (2005), *Science*, *310*, 1317–1321.

Stow, D., Hernandez-Molina, F.J., Alvarez Zarikian, C.A., and Expedition *339* Scientists (2012). Mediterranean outflow: Environmental significance of the Mediterranean Outflow Water and its global implications. *IODP Preliminary Report*, *339*, doi:10.2204/iodp.pr.339.2012.

Stumpf, R., M. Frank, J. Schönfeld, and B. A. Haley (2011). Climatically driven changes in sediment supply on the SW Iberian shelf since the Last Glacial Maximum. *Earth and Planetary Sc. Lett.*, *312*, 80–90.

Stumpf, R., M. Frank, J. Schönfeld, and B.A. Haley (2010). Late Quaternary variability of Mediterranean Outflow Water from radiogenic Nd and Pb isotopes. *Quaternary Sci. Rev.*, *29*, 2462–2472.

Thomson, J., S. Nixon, C. P. Summerhayes, E. J. Rohling, J. Schonfeld, R. Zahn, P. Grootes, F. Abrantes, L. Gaspar, and S. Vaqueiro (2000). Enhanced productivity on the Iberian margin during glacial/interglacial transitions revealed by barium and diatoms, *J. Geol. Soc.*, *157*, 667–677.

Thomson, J., S. Nixon, C. P. Summerhayes, J. Schonfeld, R. Zahn, and P. Grootes (1999). Implications for sedimentation changes on the Iberian margin over the last two glacial/interglacial transitions from (^{230}Th$_{excess}$)$_o$ systematics, *Earth Planet. Sci. Letts.* *165*, 255–270.

Tzedakis, P. C., K. H. Roucoux, L. de Abreu, and N. J. Shackleton (2004), The duration of forest stages in southern Europe and interglacial climate variability, *Science*, *306*, 2231–2235, doi:10.1126/science.1102398.

Tzedakis, P.C., H. Pälike, K. H. Roucoux, and L. de Abreu (2009), Atmospheric methane, southern European vegetation and low-mid latitude links on orbital and millennial timescales, *Earth Planet. Sci. Lett.*, *277*, 307–317.

Vautravers, M. J., and N. J. Shackleton (2006), Centennial-scale surface hydrology off Portugal during marine isotope stage 3: Insights from planktonic foraminiferal fauna variability, *Paleoceanography*, *21*, PA3004, doi:10.1029/2005PA001144.

Voelker, A.H.L., and L. de Abreu (2011), A review of abrupt climate change events in the northeastern Atlantic Ocean (Iberian Margin): Latitudinal, longitudinal, and vertical gradients. In: Abrupt Climate Change: Mechanisms, Patterns, and Impacts, *Geophysical Monograph Series*, *193*, American Geophysical Union, Washington, D. C., pp.15–37.

Weltje, G.J., and R. Tjallingii (2008), Calibration of XRF core scanners for quantitative geochemical logging of sediment cores: Theory and application, *Earth and Planetary Sc. Lett.*, *274*, 423–438.

Ziegler, M., T. Jilbert, G. J. de Lange, L. J. Lourens, and G.-J. Reichart (2008), Bromine counts from XRF scanning as an estimate of the marine organic carbon content of sediment cores, *Geochem. Geophys. Geosyst.*, *9*, Q05009, doi:10.1029/2007GC001932.

Zonneveld, K. A. F., et al. (2010), Selective preservation of organic matter in marine environments; processes and impact on the sedimentary record, *Biogeosciences*, *7*, 483–511.